Progress In Electromagnetics Research C, Vol. 171, 515–528, 2026

PIER C

(Received 29 April 2026, Accepted 1 June 2026, Scheduled 21 July 2026)

Analysis of Electromagnetic Characteristics and Temperature Field of 6-Pole 36 Slot Permanent Magnet Synchronous Motor with Nonuniform Air Gap

Xiaojun Wang[1], Hongbin Yin[1,2,*], Mingyang Luo[1], Zhongbiao Li[1], Xinfei Li[1], and Pengcheng Zheng[1]

[1]*School of Transportation and Vehicle Engineering, Shandong University of Technology, Zibo 255049, China*
[2]*Shandong Provincial Key Laboratory of Integrated Design and Intelligentization for New Energy Vehicles, Zibo 255000, China*

ABSTRACT: To reduce the cogging torque of a 6-pole 36-slot permanent magnet synchronous motor, a method using a nonuniform air gap is proposed. By establishing the sinusoidal distribution subdomain model of the rotor with a nonuniform air gap and combining the energy method with Fourier decomposition, the analytical expressions of cogging torque under the conditions of uniform and nonuniform air gaps are derived. Electromagnetic and thermal performance simulations of uniform and nonuniform air gap motors were performed using ANSYS software. The influence of the nonuniform air gap on the motor's electromagnetic and thermal performance was analyzed by comparing simulation results. First, the finite element model of the motor was established in ANSYS Maxwell to analyze its electromagnetic performance under no-load and load conditions. The magnetic flux density distribution, no-load back EMF, output torque, cogging torque, core loss, copper loss, and eddy current loss of the permanent magnet were analyzed, and the rationality of using a nonuniform air gap was verified. The loss results obtained by the electromagnetic simulation were used as the heat source. It was imported into the steady-state thermal analysis module of ANSYS Workbench to build a three-dimensional temperature-field simulation model of the motor. Through a comparative analysis of electromagnetic performance and steady-state temperature rise results, it was confirmed that the design of the 6-pole 36-slot permanent magnet synchronous motor met the predetermined performance indicators and thermal safety requirements, and the feasibility of the nonuniform air-gap design scheme was verified.

1. INTRODUCTION

Owing to its high power density, high efficiency, and excellent dynamic response characteristics, the Permanent Magnet Synchronous Motor (PMSM) has emerged as a core power source for high-end equipment, such as new energy vehicles, industrial servo systems, and wind power generation. Extensive in-depth research has been conducted by scholars on motor design and thermal performance. In the field of PMSM design, Ref. [1] proposed a nonuniform air-gap rotor design based on the eccentricity principle. By aligning the minimum air gap with the direct (d) axis and the maximum air gap with the quadrature (q) axis, the motor's electromagnetic performance was effectively improved. Meanwhile, an analytical model of the no-load air-gap magnetic field based on the magnetic potential admittance method was established, and prototype tests verified the effectiveness of the proposed design in enhancing electromagnetic performance. Ref. [2] designed a 6-pole 36-slot interior permanent magnet synchronous motor (IPMSM) structure with a nonuniform air gap. A multi-objective hierarchical design method was adopted to configure structural parameters of the stator and rotor, and a comprehensive analysis of the loss, temperature distribution, and irreversible demagnetization of the fabricated motor was conducted. The test results verified the rationality of the proposed design scheme in reducing torque ripple and electromagnetic vibration. Aiming at the vibration and noise issues under high-speed operating conditions, Ref. [3] put forward a nonuniform air gap structure design with a micro-grooved surface. The micro-groove parameters were determined through extensive finite element simulations, and prototype tests demonstrated that the proposed design significantly reduced the total harmonic distortion (THD) of the no-load back electromotive force (back-EMF) and torque ripple, with the vibration acceleration under full-throttle conditions reduced by approximately 10 dB compared with the target limit. From the perspective of topology optimization, Ref. [4] developed a PMSM design paradigm adopting a rotationally asymmetric structure. Through a population-based multi-dimensional design method, the synergistic improvement of the constant power speed range (CPSR) and torque density was achieved, and three-dimensional finite element analysis (3D FEA) verified the superior performance of the asymmetric design over the traditional surface-mounted PMSM structure. To address the design challenges under high-speed and extreme operating conditions, Ref. [5] comprehensively considered demagnetization characteristics and mechanical properties of rare-earth permanent magnets in the design of high-speed PMSMs. The rotor dimensions were derived based on the variation of operating temperature, and the stator design

* Corresponding author: Hongbin Yin (yinhongbin@sdut.edu.cn).

was completed accordingly. The influence of operating temperature and armature reaction field on irreversible demagnetization was validated via electromagnetic finite element analysis, and prototype tests confirmed the effectiveness of the proposed design method. Ref. [6] focused on cryogenic environments and designed a low-temperature PMSM for liquefied natural gas (LNG) submersible pumps. In view of the significant changes in the magnetoelectric properties of materials under the operating condition of $-161°$C, a redesign was carried out on the basis of the conventional motor design, and finite element analysis and prototype tests verified the rationality of the proposed scheme under extreme temperature conditions. For the specific driving conditions of campus patrol electric vehicles, Ref. [7] determined the rated power and speed range of the drive motor based on operating data collected from real vehicles. The motor's initial design was completed accordingly, and targeted optimization was conducted for the permanent magnet structure, air-gap length, and stator core geometry. The test results verified the adaptability of the proposed design to specific operating conditions. Based on flat wire winding technology, Ref. [8] designed the structure and dimensional equations of an IPMSM for traction drive, established a mathematical model considering iron loss, and completed the optimization of the magnetic pole structure. Through finite element simulation, efficiency map analysis, combined with vibration and noise analysis, as well as modal analysis, the comprehensive performance of the proposed design in improving power density, widening the high-efficiency range, and suppressing electromagnetic vibration was verified. For the rail-mounted belt-driven elevator system, Ref. [9] completed the electrical and magnetic circuit modeling of a 4.5 kW inner-rotor PMSM under the volume constraint defined by the mechanical design. Key parameters, including the slot opening, magnet thickness, pole arc coefficient, stator tooth thickness, and air gap, were optimized, and the design goals of low torque ripple and high efficiency were achieved by combining the segmented skewed pole technology of the permanent magnet. Prototype tests verified the reliability of the proposed design scheme. For the 15 kW, 120 k rpm high-speed PMSM for gas compressors, Ref. [10] determined the preliminary structure by comparing two rotor topology schemes and carried out a detailed design for the winding wire diameter, stator core size, and permanent magnet thickness, which ultimately achieved effective reduction of windage and friction loss and significant improvement of power density.

In the research on thermal performance of permanent magnet synchronous motors (PMSMs), as motor power density continues to rise, thermal management has become a critical factor that ensures the operational reliability of motors. Aiming at the excessive eddy current loss and temperature rise caused by the multi-permanent magnet structure, this paper established a multi-physics coupling simulation model for analysis. Ref. [11] proposed a permanent magnet motor with combined magnetic poles. A subdomain model of the rotor with a nonuniform air gap was established based on Laplace's equation, and the analytical expression of eddy current loss was derived. The temperature field analysis was carried out through the equivalent thermal network method and magneto-thermal bidirectional coupling method, and experiments verified the effectiveness of the nonuniform air-gap structure in reducing loss and suppressing temperature rise. To address the pain points of high loss density and difficult heat dissipation of high-speed PMSMs, Ref. [12] took amorphous alloy stator core and interior permanent magnet rotor as the research objects, analyzed magnetic flux density trajectories under different power supply modes, and proposed an electromagnetic-thermal iterative calculation method, which provided a theoretical basis for motor temperature rise suppression. For megawatt-level high-speed PMSMs, Ref. [13] systematically studied the electromagnetic and mechanical losses of the motor using the finite element method, proposed a composite rotor structure to enhance the anti-demagnetization capability, and analyzed the temperature distribution law of the motor through the fluid-thermal coupling method. Prototype experiments verified the accuracy of the established numerical model. Ref. [14] established an electromagnetic-thermal-fluid multi-field bidirectional coupling model, where the loss calculated by the two-dimensional transient finite element method was loaded as the heat source, and the material physical properties were updated according to the real-time temperature distribution. Tests on an 8 kW prototype verified significant advantages of the bidirectional coupling model in improving calculation accuracy. Ref. [15] established an accurate electromagnetic simulation model by obtaining the iron-loss curves of silicon steel sheets at different frequencies and the B-H curves of permanent magnets at different temperatures, and comparatively analyzed the influence of unidirectional and bidirectional coupling models on the temperature field and electromagnetic characteristics of the motor. The experimental results showed that the calculation results of the bidirectional coupling model were in better agreement with the measured values, as it fully considered the interaction between the electromagnetic and temperature fields. Aiming at the problems of high loss and low efficiency of fractional-slot PMSMs for automotive applications, Ref. [16] proposed three novel rotor magnetic circuit structures, which reduced the total motor loss to 59% of that of the original structure. Meanwhile, a three-dimensional transient temperature-field simulation model was established, which provided an important reference for the thermal design of wide-speed-range automotive motors. For IPMSMs, Ref. [17] proposed a thermal equivalent circuit model considering both rotor iron loss and permanent magnet eddy current loss. The heat source distribution was accurately calculated by a numerical method, and a thermal network model was constructed based on thermal resistance and heat capacity parameters. Temperature tests on a 25 kW prototype verified the effectiveness of the proposed model in improving thermal estimation accuracy. To solve the heat dissipation problem of high-speed PMSMs for air compressors in hydrogen fuel cell systems, Ref. [18] established an indirect magneto-thermal coupling analysis model and comparatively analyzed the cooling efficiency of axial water channels and circumferential parallel water channels. The research results indicated that the axial cooling water channel scheme has better applicability for centrifugal air compressor motors. Ref. [19] established an electromagnetic-thermal dynamic coupling model of automotive PMSMs under the maximum torque per ampere (MTPA) and field-weakening control strategies, investigated the influence of temperature variation on the electromagnetic parameters and output performance of the motor, and revealed the complex mechanism that temperature rise leads to the reduction of electromagnetic torque ripple, the increase of total loss, and the decrease of efficiency. For high-speed amorphous alloy PMSMs, Ref. [20] proposed an electromagnetic-thermal bidirectional coupling method considering the assembly gap between components. The loss was calculated, and the material physical properties were updated in real time through the three-dimensional transient finite element method. Tests on a 15 kW prototype verified the superiority of the proposed bidirectional coupling method in improving the calculation accuracy of loss and temperature rise.

This study investigates a 6-pole, 36-slot permanent magnet synchronous motor (PMSM). A nonuniform air-gap design is proposed to enhance the motor's electromagnetic performance. Based on its performance specifications and key structural parameters, a finite element model was established to obtain the electromagnetic characteristics and key loss distribution under rated operating conditions. Utilizing the loss data derived from the electromagnetic simulation, a steady-state thermal analysis was conducted to observe the temperatures of the permanent magnets and windings. A comparative analysis of the simulation results for both uniform and nonuniform air-gap configurations was performed to validate the rationality of the design.

2. MOTOR PARAMETERS

A PMSM primarily consists of stator windings, a stator core, permanent magnets, and a rotor core. Based on the position of the permanent magnets within the rotor, PMSMs can be categorized into two main structural types: surface-mounted and interior-mounted. In the interior-mounted type, the magnets are embedded inside the rotor. This configuration offers robust magnet installation, resulting in enhanced safety and reliability during high-speed operation, which is why it is the predominantly adopted rotor structure.

This study investigates a 22 kW, 1500 r/min PMSM designed for electric vehicles. The main structural design parameters are listed in Table 1. Two sets of parameters were used in the simulations for this study. Apart from the difference in the rotor outer diameter, all other parameter values and simulation settings remained identical between the two sets.

TABLE 1. Main structural design parameters of the motor.

Parameters	Values (mm)
Rotor inner diameter	47
Rotor outer diameter	168,165
Permanent magnet thickness	4.6
Permanent magnet width	35
Magnetic bridge width	1
Stator inner diameter	169.4
Outer diameter of stator	260
Slot depth	1.5
Slot width	3.5
Parallel tooth width	6.5
Winding diameter	0.5

3. ANALYSIS OF ELECTROMAGNETIC AND THERMAL PROPERTIES OF MOTORS

3.1. Mathematical Model of Electromagnetic Characteristics and Loss Calculation

3.1.1. Mathematical Model of Electromagnetic Characteristics

When the motor rotor is driven into rotation by a prime mover, the main magnetic field generated by the permanent magnets rotates with it, creating relative motion with the stationary stator windings. According to Faraday's law of electromagnetic induction, this changing magnetic flux linkage induces an electromotive force (EMF) in the stator windings. Under this open-circuit condition with no armature current, there is no armature reaction magnetic field. Therefore, the induced EMF is generated solely by the permanent magnets. Its waveform is determined by the spatial distribution of the permanent magnet field and winding configuration, ideally approximating a sinusoidal wave under an optimal design. The calculation is as follows

$$E_0 = \sqrt{2}\pi f N k_w \Phi_f \tag{1}$$

where E_0 is back-EMF; f is the supply frequency of the motor operation; N is the number of turns per phase, a fundamental parameter in winding design; k_w is the winding factor, used to account for the influence of winding structure on the induced EMF; Φ_f is the magnetic flux per pole, reflecting the strength of the air-gap magnetic field.

Cogging torque is a type of detent torque present under no-load conditions. It is caused by the interaction between the permanent magnet field and the slotted structure of the stator core. As the rotor rotates, the stator slots cause a periodic variation in the air-gap magnetic reluctance. This results in changes in the permanent magnet field energy with rotor position, thereby generating torque pulsations.

Compared with the case of a uniform air gap, the nonuniform air-gap rotor structure alters the air-gap flux density distribution, which inevitably affects the magnitude of the cogging torque. A mathematical model for the cogging torque of the PMSM was established based on the energy method, and the relationship between rotor eccentricity and cogging torque is analyzed as follows.

$$T_{cog}(\alpha) = -\frac{\partial E}{\partial \alpha} \tag{2}$$

$$E = \frac{1}{2\mu_0}\int_V B^2(\theta, \alpha)\mathrm{d}V \tag{3}$$

where E is the magnetic field energy storage of the motor that is related to the relative position angle α between the stator and rotor; μ_0 is the permeability of free; V is the spatial volume; B is the air-gap flux density; θ is the angle between the air-gap flux density vector and the magnetic pole centerline.

The mathematical model describing the distribution of air-gap flux density along the rotor surface is given by:

$$E = \frac{1}{2\mu_0} \int_V B_r^2(\theta) \left[\frac{h_m(\theta)}{h_m(\theta) + \delta(\theta, \alpha)} \right]^2 \mathrm{d}V \tag{4}$$

where B_r is the remanent flux density; $h_m(\theta)$ is the thickness of the permanent magnet in the magnetization direction at the position defined by angle θ from the magnetic pole centerline; $\delta(\theta, \alpha)$ is the distribution function of the effective air-gap length along the circumferential direction.

By performing Fourier expansion on B_r^2 and $\frac{h_m(\theta)}{h_m(\theta)+\delta(\theta,\alpha)}$:

$$B_r^2(\theta) = B_{r,0} + \sum_{n=1}^{\infty} B_{r,n} \cos 2np\theta \tag{5}$$

$$\frac{h_m(\theta)}{h_m(\theta) + \delta(\theta, \alpha)} = G_0 + \sum_{n=1}^{\infty} G_n \cos nz(\theta + \alpha) \tag{6}$$

Substituting Equations (5) and (6) into Equation (4) and then substituting the resulting Equation (4) into Equation (2) yields the expression for the motor's cogging torque. For a PMSM with a uniform air gap, Equation (4) is reduced to

$$T(\alpha) = \frac{\pi z L_a}{4\mu_0} \left(R_1^2 - R_2^2 \right) \sum_{n=1}^{\infty} n G_n B_{r,_{nz/2p}} \sin nz\alpha \tag{7}$$

where L_a is the axial length of the motor, and $B_{r,nz/2p}$ represents the Fourier series coefficient of the uniform air-gap flux density.

For a PMSM with a nonuniform air gap, Equation (2) becomes

$$T(\alpha) = \frac{\pi L_a}{4\mu_0} \left(R_1^2 - R_2^2 \right) \sum_{n=1}^{\infty} n G_n B_{r,n} \sin n\alpha \tag{8}$$

where $B_{r,n}$ represents the Fourier series coefficient of the nonuniform air-gap flux density.

The output torque is generated when a symmetric three-phase alternating current is applied to the stator windings, producing a rotating armature magnetic field. The calculation formula is as follows:

$$T_e = \frac{3}{2} p \left[\Psi_f i_q + (L_d - L_q) i_d i_q \right] \tag{9}$$

where p is the number of pole pairs; ψ_f is the permanent magnet flux linkage; i_d and i_q are the components of the stator current on the d-axis and q-axis; l_d and l_q are d-axis and q-axis synchronous inductances, respectively.

3.1.2. Loss Calculation

The temperature rise in a motor is primarily caused by its operational losses. Therefore, loss calculation is a prerequisite for thermal field analysis. The total losses consist of two parts: electromagnetic losses and mechanical friction losses. Electromagnetic losses include winding copper loss, core losses in the stator and rotor, and eddy current loss in permanent magnets. Mechanical friction losses encompass bearing friction loss and rotor windage loss.

Copper loss in windings constitutes a major portion of the total motor loss. It is calculated using the following formula:

$$P_{cu} = 3I^2 R \tag{10}$$

where I is the phase current, and R is the winding resistance.

The stator core loss primarily comprises three components: eddy current loss in the laminations, hysteresis loss owing to the ferromagnetic material properties, and additional (or excess) loss. Based on the Bertotti core loss separation model, the iron loss in the stator can be calculated as follows:

$$P_{Fe} = P_h + P_e + P_c \tag{11}$$

where P_{Fe} is the total iron loss, P_h the hysteresis loss, P_e the eddy current loss in the silicon steel laminations, and P_c the additional (excess) loss.

During motor operation, the permanent magnets are subjected to a time-varying magnetic field, which induces an electromotive force and consequently generates circulating eddy currents. These currents cause power loss along their paths, leading to an increase in the temperature of the magnets. The eddy current loss in permanent magnets was calculated using the following formula:

$$P_{pm} = \sum_n \left(\int \frac{|J_n|}{2\sigma} \mathrm{d}V \right) \tag{12}$$

where P_{pm} is the eddy current loss in the permanent magnets, J_n the eddy current density, and σ the electrical conductivity.

Windage loss refers to the friction loss generated between the high-speed rotating rotor and the surrounding air. It can be expressed as:

$$P_f = 17 D_r^2 n_1 l_r \times 10^{-9} \tag{13}$$

where P_f is the windage loss, n_1 the rotational speed of the rotor, D_r the rotor outer diameter, and l_r the axial length of the rotor.

The specific loss values under the rated operating conditions obtained from the simulation are presented in Table 2.

3.2. Electromagnetic and Thermal Performance Analysis Model for Electric Motors

3.2.1. Electromagnetic FEM Model and Settings

The procedure for establishing the finite element model (FEM) of the permanent magnet synchronous motor is outlined as follows:

Based on the motor's structural parameters, a 2D motor model was created using software AutoCAD. This model was

TABLE 2. Losses in various parts of the motor.

Loss Part	Stator Core Loss	Rotor Core Loss	Permanent Magnet Loss	Copper Loss
Value (nonuniform air gap) (W)	34.9	12.3	3.4	124.4
Value (uniform air gap) (W)	32.1	10.3	2.8	124.4

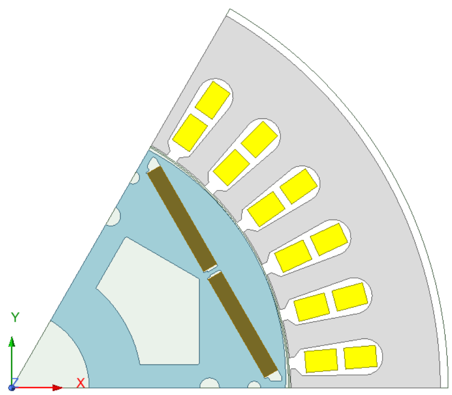

FIGURE 1. 1/6 motor model.

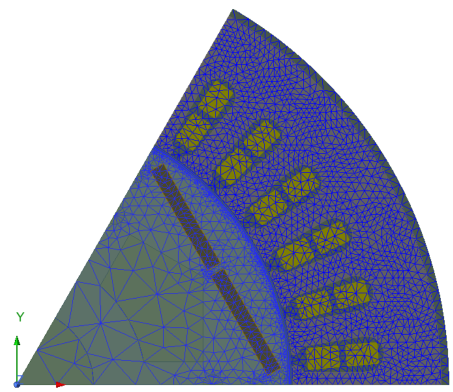

FIGURE 2. Mesh generation results.

then imported into the Maxwell simulation software in .dxf or .dwg format. To enhance simulation speed and computational efficiency, a 1/12 sector model of the motor was selected for the analysis.

The stator and rotor cores were assigned DW350 material. The permanent magnets were defined as N35UH, and the windings were assigned copper properties. The stator and rotor solution regions were set to air. Fig. 1 illustrates the resulting 1/6 sector simulation model of the motor.

Before electromagnetic simulation is conducted, the permanent magnet synchronous motor (PMSM) model needs to be meshed, and the boundary conditions and winding parameters need to be set reasonably.

The main contents of transient field analysis are the time and frequency domains. The solver was set as a transient field, and the coordinate system was rectangular. To improve the accuracy of the simulation results and consider the simulation speed, the air gap was divided into four mesh layers. According to the above parameter settings, the air gap is divided into layers. The results of the division are shown in Fig. 2.

In the electromagnetic simulation of the PMSM, both the master-slave and Dirichlet (zero flux) boundary conditions must be configured. The master-slave boundary condition was applied perpendicular to the magnetic flux lines. Combined with subsequent periodic sector settings, this allows for the simulation of the full motor model using a minimal computational domain. The Dirichlet boundary condition ($\Phi = 0$) is applied to constrain the magnetic flux lines to be parallel to the boundary, preventing them from crossing it. Subsequently, a motion band (or rotating region) is assigned and set to the rotational property. Because the motor model was imported from CAD, the winding properties needed to be defined. Windings for phases A, B, and C are added separately, with their respective current directions specified.

3.2.2. Multi-Physical Field Models for the Temperature Field of Magnetocaloric Coupled Motors and Settings

A magnetic-thermal multiphysics coupling approach was employed. The motor losses were directly mapped as heat sources onto the temperature field, enabling an integrated coupled simulation analysis of the electromagnetic and thermal fields under rated operating conditions.

An electric motor constitutes a complex coupled system with intricate interactions among multiple physical fields. To simplify the simulation process, the following assumptions are made:

(1) The skin effect of currents was neglected:

This study focuses on a 6-pole PMSM traction motor rated at 1500 r/min. The fundamental electrical frequency:

$$f_1 = \frac{pn}{60} \tag{14}$$

where p is the number of poles of the motor ($p = 3$), and n is the mechanical speed. The fundamental frequency of the stator winding of the motor is 75 Hz under the rated working condition.

To verify the skin effect under Pulse Width Modulation (PWM) supply, the skin depth in copper is:

$$\delta = \sqrt{\frac{\rho}{\pi f \mu_0}} \tag{15}$$

where ρ is the copper resistivity at the working temperature (take $2.26 * 10^{-8}\,\Omega \cdot \text{m}$ under the rated working condition of 100°C); μ_0 is the vacuum permeability ($4\pi * 10^{-7}$ H/m); f is the current frequency. The skin depth of the copper conductor at the fundamental frequency is about 8.7 mm; combined with

TABLE 3. Motor materials and their selected properties.

Component	Material	Thermal Conductivity (W/m·K)	Specific Heat Capacity (J/kg·K)	Density (kg/m^3)
Stator Core	DW350	30	450	7650
Winding	Copper	400	385	8900
Permanent Magnet	NdFeB	8	450	7500
Housing	Aluminum Alloy	160	900	2700

the typical carrier frequency (8 kHz) of the on-board traction inverter, the skin depth corresponding to the carrier subharmonic is about 0.84 mm.

The stator uses 0.5 mm diameter copper wire, much smaller than the skin depth. Given the high carrier ratio (> 100), the additional copper loss from carrier and higher harmonics is less than 2% of the total copper loss. Including proximity effects, the total loss contribution is under 3%, which is acceptable for this study.

(2) The influence of temperature variation on material parameters was not considered.

(3) All materials were assumed to be isotropic.

(4) Thermal radiation effects of the motor were ignored.

(5) The electromagnetic field was governed by Maxwell's Equations, formulated as follows:

$$\begin{cases} \frac{\partial}{\partial x}\left(\frac{1}{\mu}\left(\frac{\partial A}{\partial y}-\frac{\partial A}{\partial z}\right)\right)-\frac{\partial}{\partial x}\left(\frac{1}{\mu}\left(\frac{\partial A}{\partial x}-\frac{\partial A}{\partial y}\right)\right)=J-\gamma\frac{\mathrm{d}A}{\mathrm{d}t} \\ \frac{\partial}{\partial y}\left(\frac{1}{\mu}\left(\frac{\partial A}{\partial z}-\frac{\partial A}{\partial x}\right)\right)-\frac{\partial}{\partial y}\left(\frac{1}{\mu}\left(\frac{\partial A}{\partial x}-\frac{\partial A}{\partial y}\right)\right)=J-\gamma\frac{\mathrm{d}A}{\mathrm{d}t} \\ \frac{\partial}{\partial z}\left(\frac{1}{\mu}\left(\frac{\partial A}{\partial x}-\frac{\partial A}{\partial z}\right)\right)-\frac{\partial}{\partial z}\left(\frac{1}{\mu}\left(\frac{\partial A}{\partial y}-\frac{\partial A}{\partial z}\right)\right)=J-\gamma\frac{\mathrm{d}A}{\mathrm{d}t} \end{cases} \tag{16}$$

$$\begin{cases} \aleph_1 : \ A = 0 \\ \aleph_2 : \ \frac{1}{\mu}\frac{\partial A}{\partial n} = -H_i \end{cases} \tag{17}$$

where A is the magnetic vector potential, J the current density, $\aleph_1$ the Dirichlet boundary condition, $\aleph_2$ the Neumann boundary condition (natural boundary condition), H_i the tangential component of the magnetic field intensity, μ the permeability, and γ the electrical conductivity.

Based on the fundamental principles of heat transfer, the heat conduction differential equation is established in a polar coordinate system as follows:

$$\begin{cases} \frac{\partial}{\partial x}\left(\lambda_x\frac{\partial T}{\partial x}\right)+\frac{\partial}{\partial y}\left(\lambda_y\frac{\partial T}{\partial y}\right)+\frac{\partial}{\partial z}\left(\lambda_z\frac{\partial T}{\partial z}\right)=-q \\ \frac{\partial T}{\partial n}|_{s1}-\lambda\frac{\partial T}{\partial n}|_{s2}=\alpha\left(T-T_f\right) \end{cases} \tag{18}$$

where λ_x, λ_y, λ_z are the thermal conductivities along the coordinate axes; s_1 and s_2 represent the adiabatic and the dissipation surface, respectively; T_f and T are the fluid and unknown solid temperatures, respectively; α is the convective heat transfer coefficient; q is the volumetric heat source density in the solid.

As a complex system containing numerous fine structures, the motor's 3D model was reasonably simplified prior to the simulation to balance computational efficiency and solution accuracy. This simplification involved applying equivalent treatments to the winding end turns, internal insulation, and air gap. The resulting simplified geometric model is shown in Fig. 3.

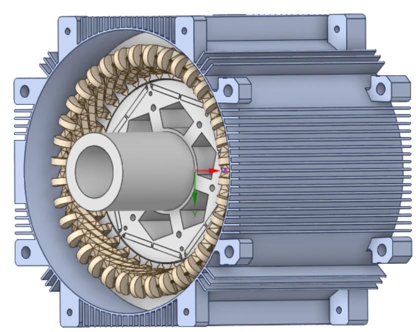

FIGURE 3. Simulation model of motor temperature field.

The motor thermal simulation model was imported into the Steady-State Thermal module of software ANSYS Workbench. The materials assigned to various components of the motor model, along with their key thermal properties, are listed in Table 4.

TABLE 4. Performance specifications of the PMSM.

Motor parameters	Values
Rated power (kW)	22
Efficiency (%)	94
Rated torque (N·m)	65
Speed (r/min)	1500
Polar logarithm	6
Number of slots	36

The following basic assumptions are made for the fluid-thermal coupling analysis of the permanent magnet synchronous motor:

(1) The motor housing outer surface is simplified as a smooth cylindrical surface.

(2) The losses in various motor components are assumed to be independent of the temperature and uniformly distributed within each component.

(3) Thermal radiation is neglected; only heat conduction and convection are considered.

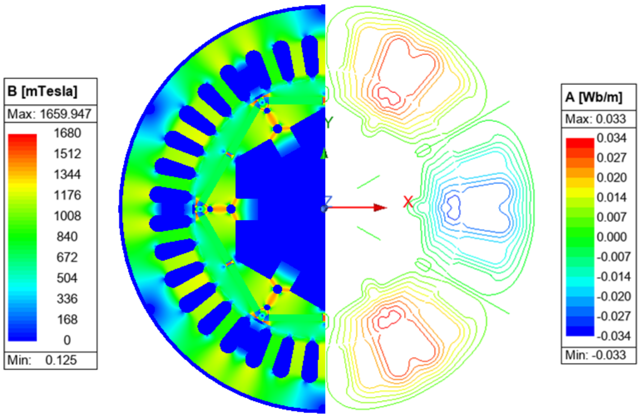

FIGURE 4. Flux distribution line and flux density of motor (nonuniform air gap motor).

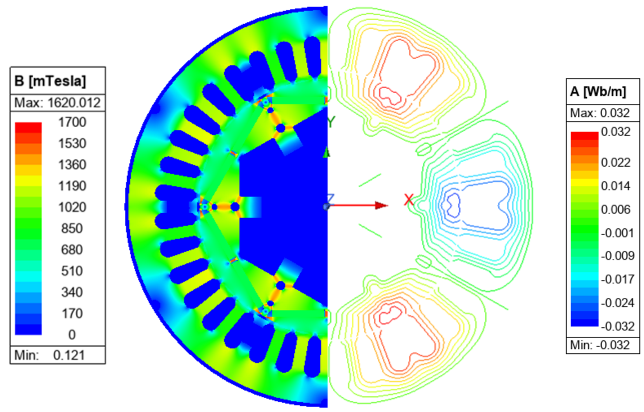

FIGURE 5. Flux distribution line and flux density of motor (uniform air gap motor).

(4) The effects of mechanical and frictional losses are disregarded.

(5) The thermal conductivity of the materials is treated as a constant, ignoring its temperature dependence.

(6) The simulation was conducted with an ambient temperature of 50°C.

Based on the losses obtained from the electromagnetic simulation, the volumetric heat generation rate (heat generation per unit volume) of the windings was calculated using.

$$R = \frac{Q}{V} \tag{19}$$

where Q is the total heat generation of the component, and V is the total volume of the component.

After defining the heat sources, the convective heat transfer coefficient on the housing surface and the cooling coefficient at the rotor ends need to be determined, which can be calculated using Equations (20) and (21).

$$\alpha_1 = 14\left(1 + 0.5\sqrt{v_1}\right)^3 \sqrt{\frac{T_0}{25}} \tag{20}$$

where v_1 is the air velocity over the housing surface (m/s), and T_0 is the air temperature at the housing surface (°C).

$$\alpha_2 = 28\left(1 + \sqrt{0.45 \cdot v_2}\,\right) \tag{21}$$

where v_2 is rotational speed of the rotor (m/s).

4. SIMULATION RESULTS

Following the establishment of the simulation models and mesh generation, electromagnetic performance simulations for the two parameter sets were conducted using ANSYS Maxwell, while the corresponding loss and temperature field simulations were performed using ANSYS Workbench.

4.1. Analysis of Electromagnetic Performance Results

4.1.1. Magnetic Flux Distribution and Magnetic Flux Density

Figures 4 and 5 show the magnetic flux lines and magnetic flux density distribution of the motor. In a PMSM with a uniform air gap, the magnetic flux lines exhibit a radially symmetric distribution, and the air-gap flux density waveform is trapezoidal with a relatively high harmonic content. In contrast, in a motor with a nonuniform air gap, the magnetic flux lines converge toward the central region of the pole shoes, resulting in an air-gap flux density waveform that more closely approximates a sinusoid, with significantly reduced harmonic components. The fundamental reason for this difference is that the nonuniform air gap introduces a spatially gradual variation in magnetic reluctance by altering the curvature of the rotor outer surface or the stator pole shoes. This guides the flux lines to distribute along the path of least reluctance, thereby optimizing the magnetic field waveform, suppressing harmonics, and mitigating localized magnetic saturation. Conversely, in a uniform air gap, where the reluctance is constant throughout, the flux lines are evenly distributed, but this leads to a pronounced distortion in the flux density waveform and higher harmonic content.

4.1.2. Air-Gap Flux Density

Figures 6 and 7 respectively show the air-gap flux density of the motor under no-load conditions. Due to the unequal arc design, slight fluctuations are present at the peaks of the waveform, which otherwise approximates a sinusoidal shape. Under no-load conditions, the air-gap flux density waveform of a motor with a uniform air gap exhibits a distinctly trapezoidal shape, characterized by rich harmonic content and significant waveform distortion. In contrast, the waveform for a motor with a nonuniform air gap more closely approximates an ideal sinusoid, with a marked reduction in high-frequency harmonic components. This difference arises because the nonuniform air gap introduces a spatially gradual variation in the air-gap length. This alters the distribution of magnetic reluctance, guiding the magnetic flux lines to converge toward the center of the poles. Consequently, the magnetic field waveform was optimized; the harmonic components are suppressed; and the localized magnetic saturation was mitigated. Conversely, the constant reluctance in a uniform air gap leads to concentrated flux density and severe waveform distortion.

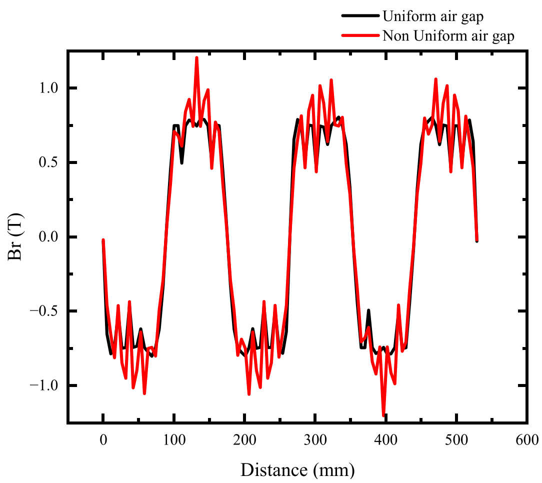

FIGURE 6. Air-gap flux density under no-load conditions.

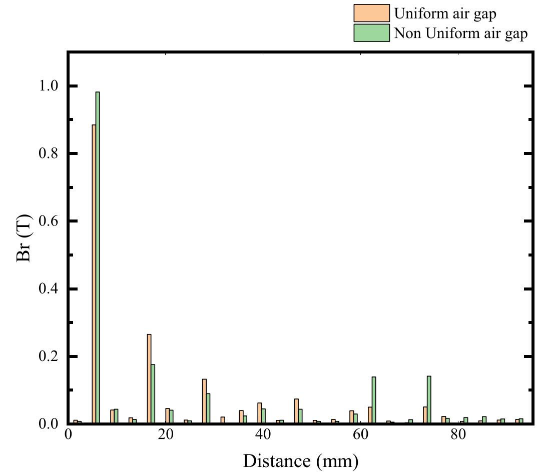

FIGURE 7. FFT analysis of air-gap flux density under no-load.

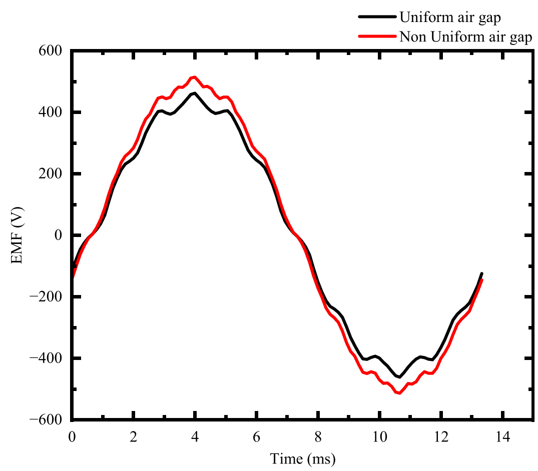

FIGURE 8. No-load back EMF.

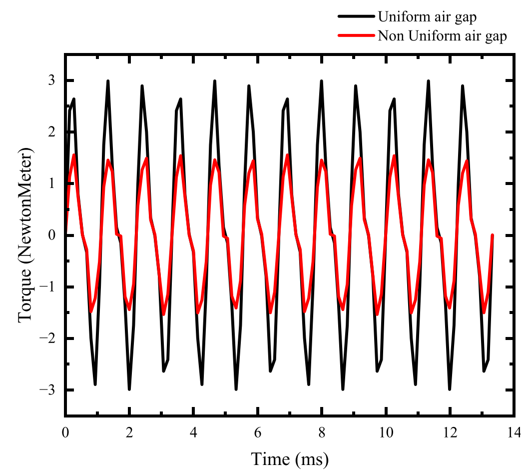

FIGURE 9. Cogging torque.

4.1.3. No-Load Back EMF

Figure 8 shows the no-load back EMF of the PMSM. The no-load back electromotive force waveform of a motor with a uniform air gap exhibits significant distortion and high harmonic content. In contrast, the EMF waveform of a motor with a nonuniform air gap more closely approximates an ideal sinusoid, with a marked reduction in high-frequency harmonics. This discrepancy arises because the back EMF is directly determined by the air-gap flux density. In a uniform air gap, the flux density waveform is trapezoidal and contains numerous harmonics. Conversely, the nonuniform air gap, through its gradual variation in length, optimizes the flux density waveform, which in turn leads to a cleaner EMF.

4.1.4. Cogging Torque

The cogging torque of the PMSM with both uniform and nonuniform air gaps was calculated using the finite element method, as shown in Fig. 9. The motor with a uniform air gap exhibits a cogging torque with a large amplitude and severe fluctuations, leading to a significant torque ripple. In contrast, for a motor with a nonuniform air gap, the cogging torque amplitude is substantially reduced; the waveform is smoother; and the torque ripple is effectively suppressed. This difference arises because the cogging torque originates from the magnetic-field interaction between the stator slots and rotor permanent magnets. In a uniform air gap, the magnetic reluctance is constant, resulting in a pronounced cogging effect and consequently large torque ripple. Conversely, the nonuniform air gap introduces a gradual variation in the air-gap length, altering the reluctance distribution. This weakens the magnetic coupling between the slots and permanent magnets and simultaneously optimizes the air-gap flux density waveform. As a result, the cogging torque was significantly decreased.

4.1.5. Electromagnetic Torque

As shown in Fig. 10, the electromagnetic torque waveform of the motor with a uniform air gap exhibits severe fluctuations and large amplitude pulsations, resulting in poor torque smoothness. In contrast, the motor's electromagnetic torque waveform with a nonuniform air gap is significantly smoother, with greatly reduced amplitude fluctuations and markedly improved

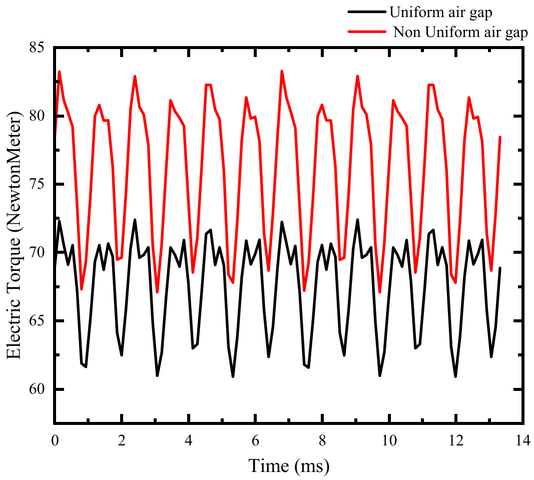

FIGURE 10. Electromagnetic torque.

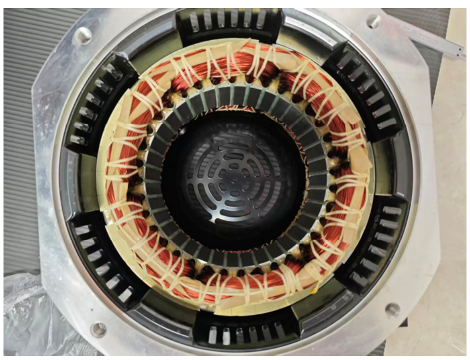

FIGURE 11. The stator of the motor.

torque smoothness. This phenomenon arises because electromagnetic torque is generated by the interaction between the air-gap magnetic field and stator current. In a motor with a uniform air gap, the distorted air-gap flux density waveform, which is rich in harmonics, leads to pronounced torque ripple. Conversely, in a motor with a nonuniform air gap, the gradual variation in air-gap length optimizes the flux-density waveform, suppressing the magnetic-field harmonics. Simultaneously, it mitigates the influence of cogging torque. Consequently, the smoothness of the electromagnetic torque is significantly enhanced.

The simulation results were consistent with the motor nameplate parameters in Table 3, indicating the accuracy of the finite element model.

The following formula was used to calculate the efficiency of the motor in both cases:

$$P_{in} = T \cdot \frac{n\pi}{30} + P_{cu} + 1.5P_{fe} + 1.5P_{eddy} + 2\% \cdot T \cdot \frac{n\pi}{30} \tag{22}$$

$$\eta = \frac{P_{out}}{P_{in}} \tag{23}$$

$$P_{out} = T \cdot \frac{n\pi}{30} \tag{24}$$

FIGURE 12. The rotor of the motor.

where T is the motor output torque, P_{cu} the copper consumption, P_{fe} the iron consumption, and P_{eddy} the eddy current loss

According to Equation (23), the efficiency of the nonuniform air-gap motor is 96.51%, and the efficiency of the uniform air-gap motor is 95.8%

The stator and rotor of the motor are shown in Figs. 11 and 12, respectively.

4.2. Thermal Performance Analysis

The temperature distribution contours for the entire motor, windings, rotor, and stator under natural cooling conditions were obtained via finite element simulation, as shown in Figs. 13 to 18.

As can be seen from Figs. 13 and 14, the motor with a nonuniform air gap has a maximum temperature of 69.568°C, characterized by a gentle temperature gradient and a more uniform overall temperature distribution. In contrast, the motor with a uniform air gap shows a comparable maximum temperature of 69.538°C, but with more concentrated high-temperature regions, more pronounced local hotspots, and a steeper temperature gradient. This difference arises because the nonuniform air gap suppresses magnetic-field harmonics by optimizing the air-gap flux density waveform. This reduces additional losses and leads to a more uniform loss distribution, thereby facilitating heat dissipation. Conversely, in the uniform air gap, harmonic losses are concentrated in localized areas, forming distinct hotspots and resulting in a less balanced temperature distribution.

As shown in Figs. 15 and 16, the simulation results indicate that for the motor with a nonuniform air gap, the maximum rotor temperature is 64.027°C, characterized by a gentle temperature gradient and a confined high-temperature region. In contrast, for the motor with a uniform air gap, the maximum rotor temperature reached 65.098°C, with a more concentrated high-temperature zone and more pronounced local hotspots. This difference is attributed to the fact that under a uniform air gap, the flux density waveform is rich in harmonics, leading to increased and concentrated rotor eddy current and hysteresis losses. These effects, coupled with the localized magnetic saturation, exacerbate the temperature increase. Conversely, the nonuniform air gap, by suppressing harmonics and dispersing

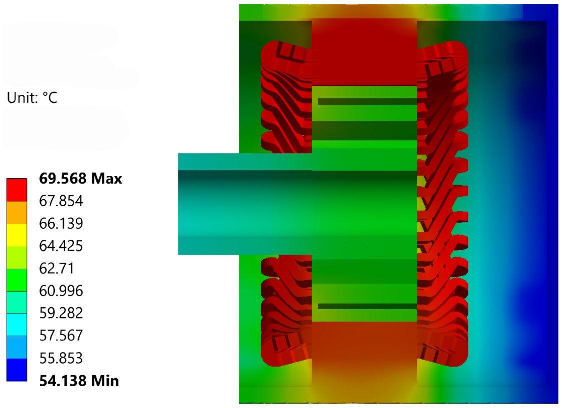

FIGURE 13. Overall motor temperature distribution (nonuniform air-gap motor).

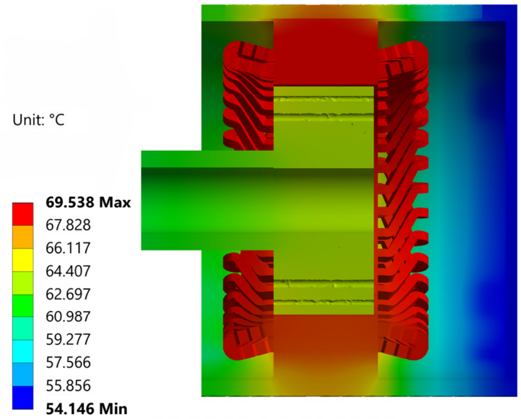

FIGURE 14. Overall motor temperature distribution (uniform air-gap motor).

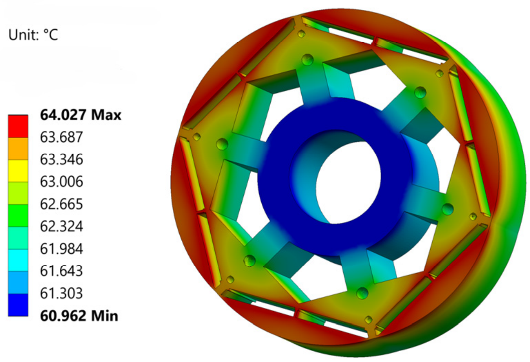

FIGURE 15. Rotor temperature distribution (nonuniform air-gap motor).

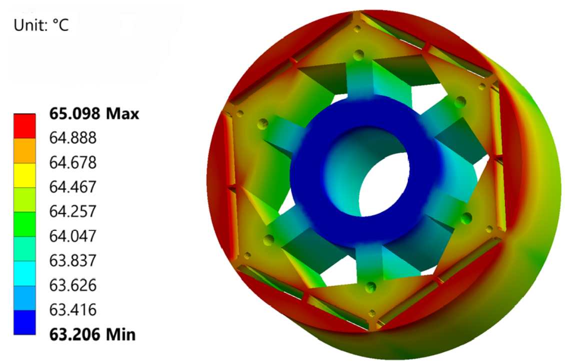

FIGURE 16. Rotor temperature distribution (uniform air-gap motor).

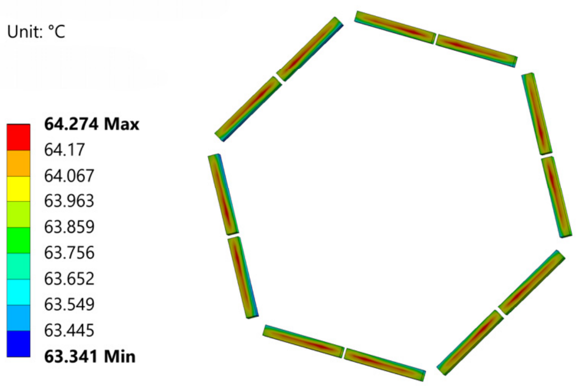

FIGURE 17. Permanent magnet temperature distribution (nonuniform air-gap motor).

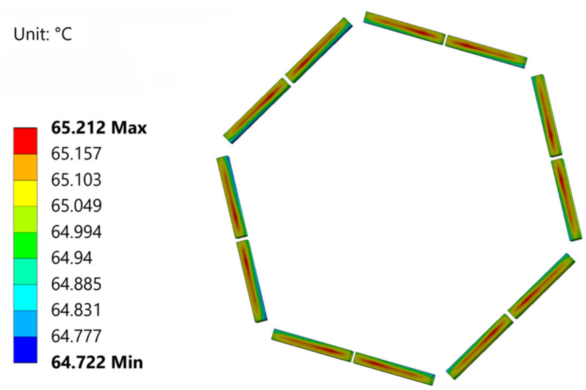

FIGURE 18. Permanent magnet temperature distribution (uniform air-gap motor).

losses, effectively alleviates local overheating in the rotor and optimizes the thermal distribution.

As shown in Figs. 17 and 18, for the motor with a nonuniform air gap, the maximum temperature of the permanent magnets is 64.274°C, characterized by a gentle temperature gradient and a more uniform temperature distribution among the magnets. In contrast, for the motor with a uniform air gap, the maximum permanent magnet temperature reaches 65.212°C, with a higher overall temperature level and more prominent local hotspots. This difference arises because the flux density waveform with a uniform air gap is rich in harmonics, leading to increased and concentrated eddy currents and hysteresis losses in the permanent magnets. These effects, combined with localized magnetic saturation, exacerbate the increase in temperature. Conversely,

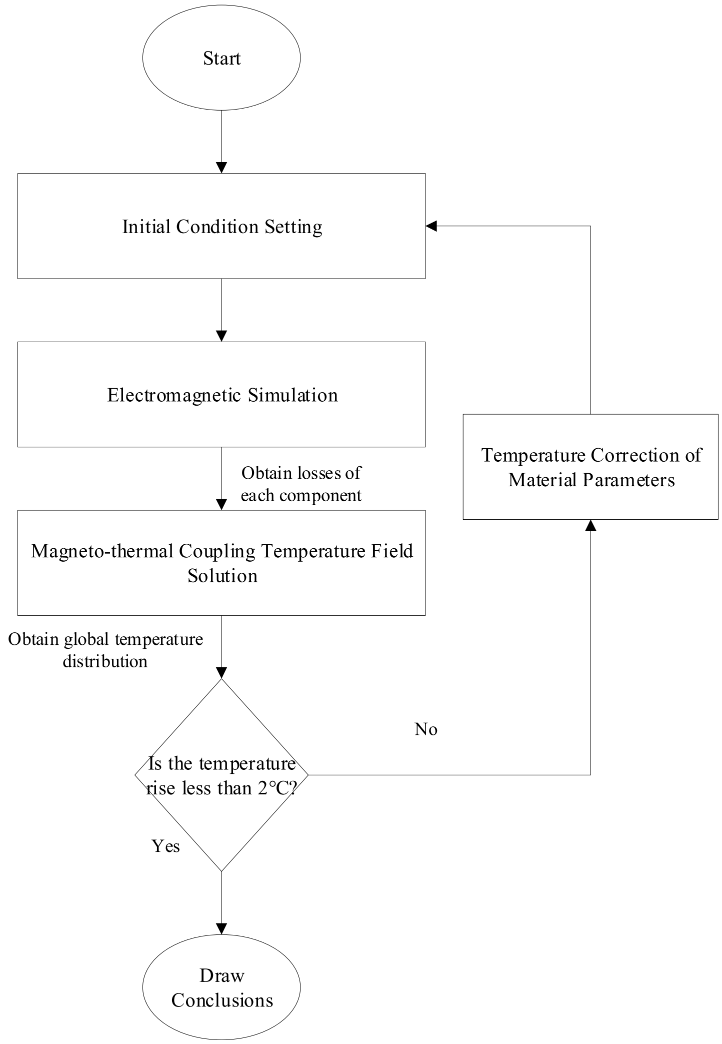

FIGURE 19. Flowchart of iterative correction for magneto-thermal coupling considering material temperature characteristics.

the nonuniform air gap, by suppressing harmonics and dispersing losses, effectively alleviates local overheating in the permanent magnets and optimizes the temperature distribution.

4.3. Magnetothermal Iterative Correction

The traditional unidirectional magneto-thermal coupling results were corrected using a sequential iterative weak bidirectional coupling method. Based on the temperature results from unidirectional coupling, the temperature's feedback effect on material electromagnetic parameters was introduced into the electromagnetic field. Self-consistent convergence between the electromagnetic field and the temperature field was achieved through multiple iterations, which strikes a balance between computational efficiency and analysis accuracy.

The ambient temperature and material reference temperature T_0 were defined, and the electromagnetic and thermophysical parameters of materials at room temperature were imported. The iteration convergence threshold εT (commonly 1–2°C in engineering practice) and the maximum number of iterations $N_{\max}$ (typically 5–10 to prevent iteration divergence) were set, with the iteration counter initialized as $k = 1$.

The electromagnetic field was solved with the current material parameters as inputs. Losses in each component, including stator copper loss, core loss, and permanent magnet eddy current loss, were extracted and applied as volumetric heat source loads for the temperature field.

The electromagnetic losses were mapped to the corresponding structural regions. Heat dissipation boundary conditions, such as convective heat transfer, contact thermal resistance, and thermal radiation, are imposed, and the global temperature distribution of the motor T^k is obtained via numerical solution.

The temperature of the current iteration T^k was compared with that of the previous iteration T^{k-1}, and the maximum temperature deviation of key components is calculated as:

$$\Delta T_{\max} = \max\left(T_i^k - T_i^{k-1}\right) \tag{25}$$

If $\Delta T_{\max} \leq \varepsilon T$ or the number of iterations reaches $N_{\max}$, the iteration converges, and the procedure proceeds to limit verification. If the convergence condition is not satisfied, the process enters the material parameter correction step; k is updated as $k = k + 1$; and the procedure returns to the electromagnetic simulation step for the next iteration.

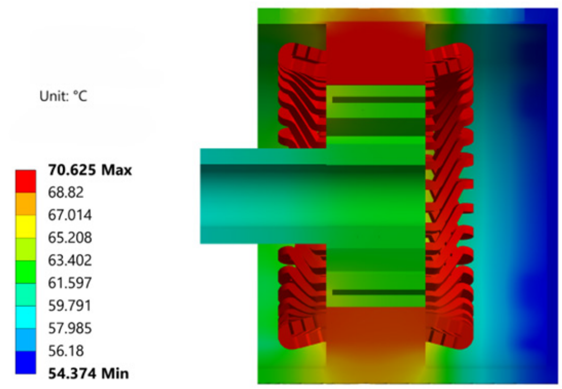

FIGURE 20. Overall motor temperature distribution after magnetothermal iteration correction (nonuniform air-gap motor).

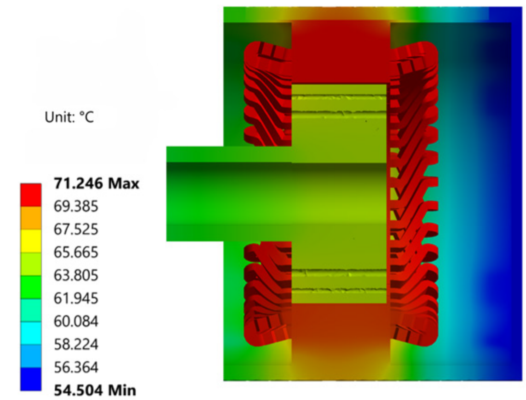

FIGURE 21. Overall motor temperature distribution after magnetothermal iteration correction (uniform air-gap motor).

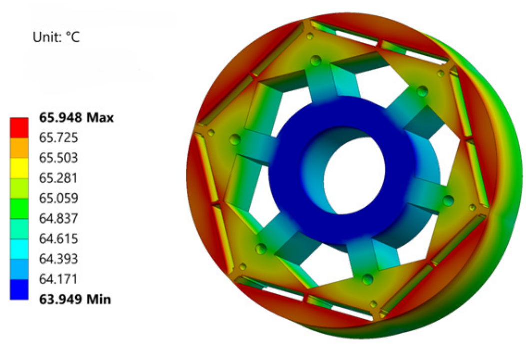

FIGURE 22. Rotor temperature distribution after magnetothermal iteration correction (nonuniform air-gap motor).

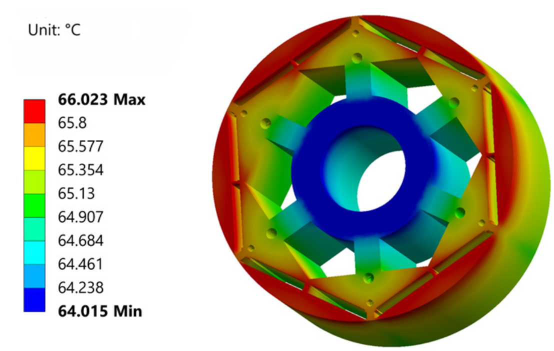

FIGURE 23. Rotor temperature distribution after magnetothermal iteration correction (uniform air-gap motor).

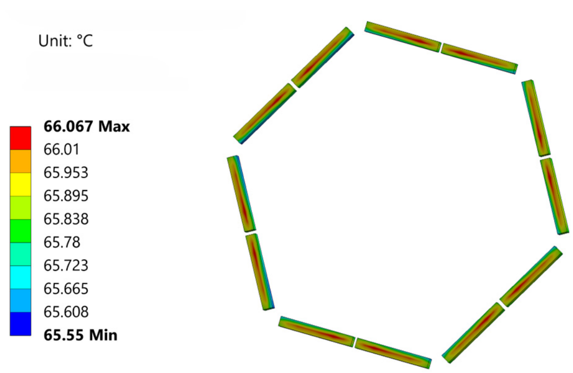

FIGURE 24. Permanent magnet temperature distribution after magnetothermal iteration correction (nonuniform air-gap motor).

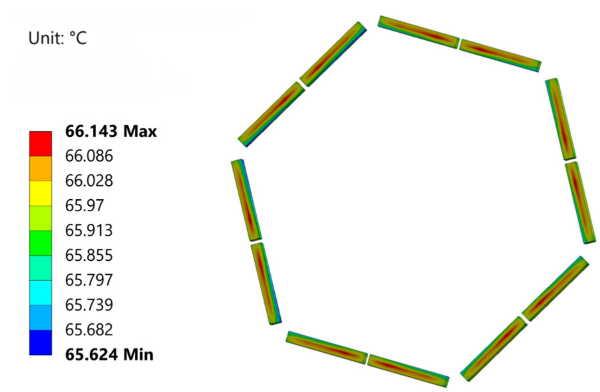

FIGURE 25. Permanent magnet temperature distribution after magnetothermal iteration correction (uniform air-gap motor).

Based on the temperature of each component obtained in the current iteration, electromagnetic parameters (winding resistivity, magnetic properties of permanent magnets, iron loss coefficients of silicon steel sheets, etc.) and the corresponding thermophysical parameters were updated according to the aforementioned material temperature correction formulas to serve as inputs for the next round of simulation. After iteration convergence, the motor temperature rise was checked against the design limit: a temperature rise $\leq 2°C$ is judged to meet the design requirements, while a temperature rise $> 2°C$ is deemed to exceed the limit, requiring optimization of the heat dissipation or electromagnetic scheme. The corrected global temperature distribution of the motor was outputted. It can supplement the error comparison with unidirectional coupling results. The flowchart of iterative correction for magneto-thermal coupling considering material temperature characteristics is shown in Fig. 19.

The results after magnetothermal iteration correction were shown in Figs. 20 to 25.

TABLE 5. Temperature of key parts before and after nonuniform air-gap correction.

Part	Temperature (before correction) (°C)	Temperature (after correction) (°C)
All motor	69.568	70.625
Rotor	64.027	65.948
Permanent	64.274	66.067

The temperatures of key parts before and after the correction of uniform air gap and nonuniform air gap are shown in Tables 5 and 6.

After iterative convergence, the temperature rise of the key heating parts of the motor is not more than 2°, indicating that the motor's temperature rise performance under this working condition meets the design requirements, and there is no risk of temperature exceeding the standard in long-term operation.

5. CONCLUSION AND PROSPECT

5.1. Conclusion

The design and simulation of a built-in permanent magnet synchronous motor (IPMSM) with 22 KW, 1500 r/min, 6 poles and 36 slots for electric vehicles were studied. A method for reducing cogging torque using a nonuniform air gap is proposed. By establishing the rotor's sinusoidal distribution subdomain model with a nonuniform air gap and combining the energy method and Fourier decomposition method, the analytical expressions of cogging torque with uniform and nonuniform air gaps are derived. Through a detailed analysis of its electromagnetic and thermal properties, the feasibility of the design was verified.

Electromagnetic simulation results demonstrated satisfactory performance: the flux distribution showed negligible leakage; the maximum flux density of 1.7 T remained below saturation; the no-load air-gap flux density was nearly sinusoidal; the no-load back EMF reached 514.04 V; the cogging torque was reduced from 2.98 N·m to 1.55 N·m by using a nonuniform air gap; and the average electromagnetic torque was 66.7163 N·m, meeting the rated torque requirement of 65 N·m. All key electromagnetic indicators met the design targets.

The thermal performance was evaluated using electromagnetic losses as heat sources under natural convection cooling. The results indicated a maximum winding temperature of approximately 69°C, with the end windings forming hotspots owing to poor heat dissipation. The permanent magnets reached a maximum temperature of 64°C with a nonuniform radial gradient. The stator teeth were hotter than the yoke, whereas the rotor operated at a lower temperature owing to smaller losses. The temperature increase of all components remained within acceptable limits for thermal safety.

In conclusion, the design of the 6-pole, 36-slot PMSM fulfills the preset performance specifications and thermal safety requirements, demonstrating its feasibility for practical engineering application.

TABLE 6. Temperature of key parts before and after uniform air-gap correction.

Part	Temperature (before correction) (°C)	Temperature (after correction) (°C)
All motor	69.538	71.246
Rotor	65.098	66.023
Permagent	65.212	66.143

5.2. Prospect

During the thermal margin assessment in this study, the dynamic coupling between material properties and temperature variation is not incorporated, which may render the obtained conclusions somewhat optimistic. Clarifying this limitation is essential for a correct understanding of the applicability of this work. Specifically, the limitations are reflected in the following two aspects:

(1) The winding copper loss is underestimated. During actual motor operation, the resistance of copper windings increases with rising temperature. Taking the typical operating condition noted by the reviewers as an example, copper resistance at an ambient temperature of 69°C increases by approximately 7% relative to the reference temperature, which directly leads to underestimated Joule heat loss, further elevates the steady-state operating temperature of the motor, and results in a lower actual thermal margin than the calculated value in this paper.

(2) The magnetic properties of permanent magnets degrade. The existing analysis fails to account for the effect of high temperature on permanent magnet materials. The remanence and coercivity of permanent magnets undergo reversible or irreversible degradation at elevated temperatures, which directly affects the electromagnetic torque output characteristics and iron loss distribution and further deviates the thermal assessment results from reality.

(3) One key limitation of this study is the lack of experimental validation for the reported results. All conclusions are based on finite element simulation, and while the model's geometry, material properties, and boundary conditions are set strictly in line with engineering standards and prior literature to ensure computational reliability, a physical prototype has not been tested due to current laboratory facility constraints. The simulated magnetic-field distribution, thermal performance, and output characteristics have not been calibrated with measured data, meaning that there may be deviations between our numerical findings and the motor's actual operating performance. The engineering applicability of the conclusions still requires further experimental confirmation. Experimental verification and model calibration based on prototype testing will be prioritized in our follow-up research.

Accordingly, the thermal margin derived in this paper can be regarded as an "ideal boundary" under the assumption of constant material properties. For scenarios requiring higher assessment accuracy, it is necessary to incorporate temperature-dependent material properties and iterative coupling calculation of electromagnetic and thermal fields, and conduct experimental research to verify the accuracy of the reported results, which also constitutes the core focus of our follow-up research.

ACKNOWLEDGEMENT

This research was funded by the Natural Science Foundation of Shandong Province (Grant No. ZR2025MS703).

REFERENCES

[1] Liu, F., X. Wang, and Z. Xing, "Design of a 35 kW permanent magnet synchronous motor for electric vehicle equipped with non-uniform air gap rotor," *IEEE Transactions on Industry Applications*, Vol. 59, No. 1, 1184–1198, 2023.

[2] Xing, Z., X. Wang, W. Zhao, X. Li, L. Xiong, and X. Zhang, "Optimization design of interior permanent magnet synchronous motor with U-shaped rotor for low-level torque ripple and electromagnetic vibration," *IEEE Transactions on Transportation Electrification*, Vol. 10, No. 1, 1995–2007, 2024.

[3] Zhang, Y., Y. Yang, Z. Y. Gu, L. Li, and T. Ma, "Multi-objective optimization for noise reduction of IPMSM based on non-uniform air gap," *IEEE Access*, Vol. 12, 48 819–48 829, 2024.

[4] Alsawalhi, J. Y. and S. D. Sudhoff, "Design optimization of asymmetric salient permanent magnet synchronous machines," *IEEE Transactions on Energy Conversion*, Vol. 31, No. 4, 1315–1324, 2016.

[5] Bang, T.-K., K.-H. Shin, J.-I. Lee, J.-H. Woo, H.-W. Cho, and J.-Y. Choi, "Design of high-speed permanent magnet synchronous machines considering thermal demagnetization and mechanical characteristic of permanent magnet," *AIP Advances*, Vol. 11, No. 2, 025129, 2021.

[6] Guo, C., S. Huang, J. Wang, Y. Feng, and Q. Wang, "Design of cryogenic permanent magnet synchronous motor for submerged liquefied natural gas pump," *IEEE Transactions on Magnetics*, Vol. 54, No. 11, 1–5, 2018.

[7] Sun, X., Z. Shi, G. Lei, Y. Guo, and J. Zhu, "Analysis and design optimization of a permanent magnet synchronous motor for a campus patrol electric vehicle," *IEEE Transactions on Vehicular Technology*, Vol. 68, No. 11, 10 535–10 544, 2019.

[8] Xu, Y., Y. Chen, Z. Fu, M. Xu, H. Liu, and L. Cheng, "Design and analysis of an interior permanent magnet synchronous motor for a traction drive using multiobjective optimization," in *International Transactions on Electrical Energy Systems*, 1–15, Wiley, 2024.

[9] Avsar, Y., A. Fenercioglu, and M. Soyaslan, "Design optimization of PM synchronous motor: Rail mounted belt drive elevator systems," *IEEE Transactions on Industry Applications*, Vol. 60, No. 1, 301–311, 2024.

[10] Zhao, F., Z. Yu, J. Cao, and L. Li, "Design and optimization of a high-speed permanent magnet synchronous machine for gas compressors," *IEEE Transactions on Magnetics*, Vol. 58, No. 2, 1–5, 2022.

[11] Ma, S., J. Ma, K. Chen, and C. Li, "Analytical modeling of eddy current losses and thermal analysis of non-uniform-air-gap combined-pole permanent magnet motors for electric vehicles," *Machines*, Vol. 12, No. 6, 377, 2024.

[12] Zhang, C., L. Chen, X. Wang, and R. Tang, "Loss calculation and thermal analysis for high-speed permanent magnet synchronous machines," *IEEE Access*, Vol. 8, 92 627–92 636, 2020.

[13] Zhang, Y., S. McLoone, W. Cao, F. Qiu, and C. Gerada, "Power loss and thermal analysis of a MW high-speed permanent magnet synchronous machine," *IEEE Transactions on Energy Conversion*, Vol. 32, No. 4, 1468–1478, 2017.

[14] Jiang, Y., D. Wang, J. Chen, Q. Zhang, and T. Xuan, "Electromagnetic-thermal-fluidic analysis of permanent magnet synchronous machine by bidirectional method," *IEEE Transactions on Magnetics*, Vol. 54, No. 3, 1–5, 2018.

[15] Jia, M., J. Hu, F. Xiao, Y. Yang, and C. Deng, "Modeling and analysis of electromagnetic field and temperature field of permanent-magnet synchronous motor for automobiles," *Electronics*, Vol. 10, No. 17, 2173, 2021.

[16] Wu, Z., S. Li, and P. Bai, "Optimized design and magneto-thermal coupling simulation analysis of automotive permanent magnet synchronous motor," *Journal of Physics: Conference Series*, Vol. 2918, No. 1, 012025, 2024.

[17] Lee, B.-H., K.-S. Kim, J.-W. Jung, J.-P. Hong, and Y.-K. Kim, "Temperature estimation of IPMSM using thermal equivalent circuit," *IEEE Transactions on Magnetics*, Vol. 48, No. 11, 2949–2952, 2012.

[18] Wang, L., Y. Wu, Y. Guo, J. Feng, and X. Peng, "Analysis of the cooling performance based on the three-dimensional magnetic-thermal coupling in high-speed permanent magnet synchronous motor," *Journal of Traffic and Transportation Engineering (English Edition)*, Vol. 12, No. 5, 1397–1414, 2025.

[19] Ge, S., J. Zhao, H. Wang, Z. Zhang, and W. Qi, "Electromagnetic thermal coupling characteristics of permanent magnet synchronous motor for electric vehicles," *Proceedings of the Institution of Mechanical Engineers, Part D: Journal of Automobile Engineering*, Vol. 239, No. 13, 6065–6083, 2025.

[20] Tong, W., R. Sun, S. Li, and R. Tang, "Loss and thermal analysis for high-speed amorphous metal PMSMs using 3-D electromagnetic-thermal bi-directional coupling," *IEEE Transactions on Energy Conversion*, Vol. 36, No. 4, 2839–2849, Dec. 2021.